Estimation of diurnal shortwave dust aerosol radiative forcing during PRIDE

Sundar A. Christopher and Jun Wang
Department of Atmospheric Sciences, University of Alabama in Huntsville, Huntsville, Alabama, USA

Qiang Ji
Science Systems and Applications, Inc., NASA Goddard Space Flight Center, Greenbelt, Maryland, USA

Si-Chee Tsay
Laboratory for Atmospheres, NASA Goddard Space Flight Center, Greenbelt, Maryland, USA

Received 23 July 2002; revised 30 October 2002; accepted 10 December 2002; published 19 July 2003.

[1] Using measured and derived aerosol properties from the Puerto Rico Dust Experiment (PRIDE), a four-stream broadband radiative transfer model is used to calculate the downward shortwave irradiance (DSWI) at the surface and the shortwave irradiance at the top of atmosphere (TOA). The results of the calculated DSWI are compared against pyranometer measurements from the Surface Measurements For Atmospheric Radiative Transfer (SMART) instrument suite at Roosevelt Road (18.20°N, 65.60°W). Using aerosol optical thickness retrievals from half-hourly geostationary satellite data (GOES 8 imager), the diurnal short wave aerosol forcing (SWARF) of dust aerosols both at the surface and TOA are calculated for the entire study area (14°N $\sim$ 26°N, 61°W $\sim$ 73°W). For selected days, the Clouds and the Earth Radiant Energy System (CERES) TOA shortwave irradiance values from Terra are compared with radiative transfer calculations. *Wang et al.* [2003] show that the satellite derived aerosol optical thickness is in excellent agreement with Aerosol Robotic Network (AERONET) values. Results of this study show that the calculated direct, diffuse and total DSWI are in excellent agreement with the corresponding SMART values with biases of 1.8%, −3.3% and 0.5% respectively, indicating that dust aerosols are well characterized in the radiative transfer model. This is well within the measured uncertainties (1.3%) and the model uncertainties (5%). The monthly mean value and standard deviation of aerosol optical thickness at 670 nm (AOT670) during PRIDE are 0.26 ± 0.13, and the corresponding monthly mean daytime SWARF values are −12.34 ± 9.62 W m^{-2} at TOA and −18.13 ± 15.81 W m^{-2} at the surface, respectively. Our results also show that if diurnal changes in aerosol optical thickness are not considered, it leads to uncertainties in SWARF of 4 W m^{-2} at the surface and 2 W m^{-2} at the TOA. The CERES TOA short wave irradiance underestimates calculated values by about 10 W m^{-2} mainly due problems in misclassification of aerosols and lack of aerosol angular dependence models (ADMs) in the current CERES algorithms. This study is among the first to demonstrate the potential of the GOES 8 imagers in retrieving aerosol optical thickness and estimating the daytime diurnal SWARF of dust, both at the TOA and surface, in low to moderate dust loading regions over the oceans. *INDEX TERMS:* 0305 Atmospheric Composition and Structure: Aerosols and particles (0345, 4801); 3359 Meteorology and Atmospheric Dynamics: Radiative processes; 3360 Meteorology and Atmospheric Dynamics: Remote sensing; *KEYWORDS:* dust aerosols, diurnal forcing, dust optical properties, forcing uncertainties, flux calculation and comparison

Citation: Christopher, S. A., J. Wang, Q. Ji, and S.-C. Tsay, Estimation of diurnal shortwave dust aerosol radiative forcing during PRIDE, *J. Geophys. Res.*, *108*(D19), 8596, doi:10.1029/2002JD002787, 2003.

1. Introduction

[2] Atmospheric aerosol particles, both natural and anthropogenic, play an important role on the radiation balance of the Earth-atmosphere system. They affect the energy budget of the Earth-atmosphere system directly by scattering and absorbing sunlight [*Penner et al.*, 1992] and indirectly by modifying the radiative properties of clouds [*Twomey*, 1977]. Dust, which is a common aerosol over the desert, can be transported to downwind areas thousands of miles away from source regions [*Prospero*, 1999; *Karyampudi et al.*,

0148-0227/03/2002JD002787$09.00

1999]; and therefore plays an important role on the regional and global radiative energy balance at the top of atmosphere (TOA) [*Hansen and Lacis*, 1990] and at the surface [*Fouquart et al.*, 1987; *Trautmann and Box*, 1995]. Although the dust aerosol radiative effect at the TOA is assumed to be one of the largest uncertainties in current global climate models (GCM) [*Intergovernmental Panel on Climate Change* (*IPCC*), 2001], equally important are their effects on the surface energy budget. The surface energy budget is closely related to surface temperature, evaporation, condensation and other boundary layer processes [*Trautmann and Box*, 1995].

[3] The radiative effects of dust aerosols at the TOA have been estimated in previous studies from satellite observations and radiative transfer models [*Fouquart et al.*, 1987; *Ackerman and Chung*, 1992; *Haywood et al.*, 2001]. Using measured size distribution and derived refractive indices [*Ackerman and Cox*, 1982], *Ackerman and Chung* [1992] estimated the aerosol properties (including single scattering albedo, $\omega_0 = 0.74$ at 0.55 μm, phase function and extinction coefficient) from Mie calculations. The calculated downward and upward shortwave irradiance values from a two-stream adding-doubling model provided good agreement with aircraft measurements. Their result also showed that the TOA shortwave aerosol radiative forcing (SWARF) of dust aerosols over oceans near the Saudi Arabian peninsula in July 1985 was $-20 \sim -60$ W m^{-2} (corresponding AVHRR retrieved aerosol optical thickness (AOT) of $0.5 \sim 1.5$ [*Rao et al.*, 1989]). This calculated SWARF was lower than the TOA irradiance values ($-40 \sim -90$ W m^{-2}) obtained from the Earth Radiation Budget Experiment (ERBE) [*Ackerman and Chung*, 1992]. Using the Total Ozone Mapping Spectrometer (TOMS) aerosol indices derived from ultra violet measurements and shortwave and longwave irradiance from ERBE data, *Hsu et al.* [2000] estimated that the SWARF of Saharan desert dust aerosols over ocean near the West Coast of Africa was approximately $-10 \sim -30$ W m^{-2} (-52 W m^{-2} per unit aerosol optical thickness) for Feb. 1985 and $-40 \sim -50$ W m^{-2} (-60 W m^{-2} per unit aerosol optical thickness) for July 1985. Using aircraft measurements, *Haywood et al.* [2001] reported dust SWARF values of -60 ± 5 W m^{-2} during April–May of 1999. Using VIRS and CERES data from Tropical Rainfall Measuring Mission (TRMM) satellite, a SWARF value of -38 W m^{-2} was also reported by *Liu et al.* [2003]. Estimates of global annual mean TOA radiative forcing due to mineral dust range from -0.46 W m^{-2} [*Sokolik and Toon*, 1996] to +0.09W m^{-2} [*Tegen and Lacis*, 1996]. The range of values and their associated uncertainties in the current estimation of dust aerosol forcing are largely due to the high spatial and temporal variations of dust aerosol properties [e.g., *Claquin et al.*, 1998].

[4] The uncertainties in characterizing aerosol properties in radiative transfer models also contribute to the discrepancy between calculated and measured downward shortwave irradiance (DSWI) at the surface [*Konzelmann et al.*, 1996]. *Charlock and Alberta* [1996] reported a 30 W m^{-2} difference between calculated and measured DSWI under clear sky conditions and concluded that the major reason for this difference is due to the inadequate characterization of aerosols in their model calculations. However, *Christopher et al.* [2000] concluded that when detailed information is available about aerosol properties, the calculated DSWI values are in good agreement with surface measurements. Since the DSWI is closely related to the surface temperature and the evaporation and condensation process in the atmosphere [*Legrand et al.*, 1992], it is important to obtain accurate dust optical properties to estimate the radiative effect of dust aerosols.

[5] One of the goals of the Puerto Rico Dust Experiment (PRIDE) was to examine the radiative impact of dust aerosols [*Reid et al.*, 2003]. During PRIDE, detailed measurements of dust properties were made both from aircraft [*Reid et al.*, 2003; *Livingston et al.*, 2003] and from ground measurements. Satellite measurements and analysis also played a key role during PRIDE [*Wang et al.*, 2003; *Levy et al.*, 2003]. In this paper, using measured dust properties and aerosol optical thickness derived from ground-based Sun photometers (SP), the DSWI at the surface was calculated from a four-stream radiative transfer model [*Liou et al*, 1988; *Fu and Liou*, 1993]. The calculated DSWI values were then compared against measurements made at the ground. A companion paper shows that the dust aerosol optical thickness at 670 nm (hereafter AOT670) retrieved from the GOES 8 imager data are in excellent agreement with the SP retrieved values [*Wang et al.*, 2003]. The satellite-retrieved AOT670 over the study region ($14°N \sim 26°N$, $61°W \sim 73°W$) are used as input to the four-stream radiative model [*Liou et al.*, 1988; *Fu and Liou*, 1993] to calculate radiative irradiance and estimate SWARF of dust aerosols both at the TOA and at the surface. The calculated TOA irradiance are also compared against the CERES derived TOA irradiance. The diurnal and monthly mean values of SWARF at TOA and surface are reported for the period of study (28 June 2000 $\sim$ 26 July 2000).

2. Data

[6] The data used in the study includes atmospheric profiles of water vapor, temperature and pressure [*Reid et al.*, 2003], the SP derived aerosol optical thickness [*Holben et al.*, 1998] at Roosevelt Road and La Paguera, DSWI (direct, diffuse, total) at the surface from Surface Measurements for Atmospheric Radiative Transfer (SMART), and the CERES ES-8 TOA irradiance [*Wielciki et al.*, 1996]. The half-hourly GOES 8 retrieved AOT670 (from 13 UTC time periods) during PRIDE [*Wang et al.*, 2003] is also used as the input to the broadband four stream radiative transfer model [*Liou et al*, 1988] to calculate the irradiance values at the TOA and surface. The GOES 8 aerosol optical thickness retrievals [*Wang et al.*, 2003] is based on a look-up table approach where the aerosol optical properties are characterized by using measured size distributions and refractive indexes inferred from light scattering and absorption measurements. The difference of monthly mean AOT670 between collocated GOES 8 retrievals and AOT670 inferred from SP measurements is within 0.02.

[7] The Sun photometer (SP) measures direct solar radiation at 0.34 μm, 0.38 μm, 0.44 μm, 0.50 μm, 0.67 μm, 0.87 μm, and 1.02 μm with approximately 0.8° full angle field and has a narrow wavelength interval of about 0.01 μm for each band [*Holben et al.*, 1998]. The measured solar radiances are then used to infer the column aerosol optical

thickness by using a cloud screening process and an inversion algorithm [*Smironov et al.*, 2000a; *Holben et al.*, 1998]. In this algorithm, the attenuation due to Rayleigh scattering and the absorption of ozone are estimated and removed. The uncertainty in the retrieved aerosol optical thickness is on the order of 0.01 [*Holben et al.*, 1998; *Smirnov et al.*, 2000a].

[8] The CERES cross-track scanner on Terra measures broadband radiances in 3 spectral channels at a nadir spatial resolution of about 20 km [*Wielicki et al.*, 1996]. The three channels include the solar reflected channel (SW) between 0.3–5 μm, the window channel (WN) between 8–12 μm, and a channel that measures total radiation from 0.3 to > 100 μm. There are two CERES instruments onboard Terra; one is used primarily in the cross track scan mode that is similar to the scanners on ERBE, and the other in the biaxial scan mode for obtaining angular dependence models (ADMs). Only the data from the cross track scan mode is used. The measured radiances are converted to irradiance at the TOA for SW and LW bands by using ADMs developed for the ERBE program [*Wielicki et al.*, 1996].

[9] During PRIDE, Precision Spectral Pyranometers (PSP) and Kipp & Zonen Thermopile Pyranometers (CM21) were used to independently measure the instantaneous total downward SW irradiances at the surface (DSWI) from 0.28 ∼ 2.8 μm. A pyranometer has an inner and an outer dome that shield the sensor and filters the radiation coming to the sensor. However, the dome also alters the balance between the sensor and the target, thus introducing an instrument offset that can be described by the "dome effect" [*Ji and Tsay*, 2000]. In addition, under ideal conditions, the response of the sensor follows Lambert's cosine law. However, due to limitations in the optics and the sensor, nonideal variations in the responses will occur. Only the total DSWI from CM21 is used in this study because it has a smaller dome effect and better cosine response. An Eppley Normal Incident Pyrheliometer (NIP) instrument was used to measure the downward direct shortwave irradiance. The downward diffuse irradiance was measured independently by two instruments; the shaded PSP and the shaded CM21. The difference between the two measurements is small (less than 1%), and therefore only the diffuse irradiance measured by the shaded PSP is used in this study. The temporal resolution of these measurements is 1 min. The data is screened for cloud cover [*Eck et al.*, 1998] and dome effects [*Ji and Tsay*, 2000] based on the temporal variations of measured irradiance and visual inspection of recorded sky images. A total of 25-days (from 28 June 2000 to 22 July 2000) of data from SMART are used in this study.

3. Methodology

3.1. Radiative Transfer Model

[10] A delta-four stream plane-parallel broadband radiative transfer model [*Fu and Liou*, 1993] was used to compute DSWI values for dust aerosols. In previous research, this model has been used to estimate the SWARF of smoke [*Christopher et al.*, 2000; *Christopher and Zhang*, 2002] and dust aerosols [*Liao and Seinfeld*, 1998]. The gas absorption, water vapor absorption, and Rayleigh scattering are included in the model calculations. The model divides the shortwave (SW) spectrum (0.2 ∼ 4 μm) into six bands 0.2–0.7, 0.7–1.3, 1.3–1.9, 1.9–2.5, 2.5–3.5, and 3.5–4.0 μm and further divides the first band (0.2–0.7 μm) into 10 subbands. For the principal atmospheric gases, the difference between the four-stream and line-by-line irradiance calculations is within 0.05% [*Fu and Liou*, 1993]. Overall, for the computations of solar irradiance covering the entire SW spectrum, the calculated values are within 5%, when compared to adding-doubling calculations [*Liou et al*, 1988].

[11] The input parameters of the model include the surface albedo, atmosphere profiles of water vapor, temperature, other atmospheric constituents (e.g., O_3) and aerosol optical properties. The output of this model includes shortwave direct, diffuse, and total irradiance, both at the top of atmosphere, the surface and in each layer of the atmosphere. Vertical profiles of temperature and water vapor from 22 days aircraft and sounding measurements during PRIDE are used in our model calculations. The default tropical profile [*McClatchey et al.*, 1971] is used only when sounding data are not available (10 July 2000 and 17 July 2000). The precipitable water content (PWC) averaged from atmospheric sounding and aircraft measurements over 18 days (when both measurements are available) are 3.75 ± 0.38 cm and 3.74 ± 0.42 cm, respectively. The PWC in the default tropical profile is 4.09 cm, slightly higher than sounding and aircraft measurements. Overall, the uncertainty of PWC is less than 0.3cm or within 10%. On the basis of our model calculations, this resulted in an uncertainty of calculated SWARF both at surface and TOA within 0.05W m^{-2} that is consistent with inferences made by previous studies [e.g., *Chou et al.*, 2002].

[12] The shortwave TOA and surface irradiance are not very sensitive to changes in ozone amount. For example, a change in ozone amount from 250 DU to 320 DU leads to changes of less than 0.5 W m^{-2} at the surface [*Chou et al.*, 2002]. Ozone retrievals from TOMS [*McPeters and Labow*, 1996] indicate that the ozone content varies from 275 DU to 300 DU over the Puerto Rico region in July 2000. Therefore the tropical ozone profile [*McClatchey et al.*, 1971] is used in all model calculations (total column ozone of 253 DU). The vertical distribution of aerosol was set as the default exponential profile where the major aerosol concentration is below 3 km. Aircraft measurements during PRIDE have shown that typical height of the dust layer is below 3 km [*Livingston et al.*, 2003; *Reid et al.*, 2003]. Previous studies have shown that TOA irradiance is not sensitive to the height of dust layer if the dust layer is below 3km [*Liao and Seinfeld*, 1998; *Chou et al.*, 2002]. The ocean surface albedo in the radiative transfer model is based on the spectral properties of ocean water scene type used in the Surface and Atmosphere Radiation Budget (SARB) program [*Charlock et al.*, 1997]. Specifically, the effect of solar zenith angle on the albedo of ocean surface is adjusted by using the following equation [*Dickinson*, 1983]

$$\rho_{(\mu)} = \rho_{(\mu_0=0.5)}(1+d)/(1+2d\mu) \quad (1)$$

where $\rho_{(\mu)}$ is albedo at the solar zenith angle $arccos(\mu)$, d is scene adjustment factor (0.41 for ocean [*Charlock et al.*,

Table 1. Dust Aerosol Properties Used in This Study[a]

Wavelength, μm	Refractive Index	ω_0	g	Normalized β_{ext}	ρ_{sfc}
		SW Bands			
0.18–0.69	1.52–0.0020 i	0.9531	0.6963	1.039	0.0787
0.69–1.30	1.51–0.0025 i	0.9668	0.6898	0.889	0.0505
1.30–1.90	1.50–0.0032 i	0.9695	0.6897	0.781	0.0163
1.90–2.50	1.50–0.0040 i	0.9683	0.6854	0.675	0.0163
2.50–3.51	1.50–0.0050 i	0.9654	0.6751	0.540	0.0163
3.51–4.00	1.50–0.0050 i	0.9673	0.6642	0.439	0.0163
		10 Subbands			
0.18–0.22	1.53–0.0033 i	0.9065	0.7419	1.358	0.082
0.22–0.24	1.51–0.0031 i	0.9169	0.7482	1.320	0.094
0.24–0.29	1.51–0.0030 i	0.9228	0.7445	1.276	0.091
0.29–0.30	1.51–0.0028 i	0.9287	0.7352	1.221	0.078
0.30–0.32	1.51–0.0025 i	0.9367	0.7279	1.190	0.072
0.32–0.36	1.52–0.0022 i	0.9447	0.7156	1.147	0.066
0.36–0.44	1.52–0.0020 i	0.9508	0.7002	1.077	0.062
0.44–0.50	1.52–0.0020 i	0.9550	0.6922	1.011	0.055
0.50–0.60	1.53–0.0020 i	0.9594	0.6788	0.962	0.044
0.60–0.69	1.53–0.0010 i	0.9803	0.6708	0.947	0.069

[a]Here ω_0 is the single scattering albedo, g is asymmetry factor, β_{ext} is the extinction cross section normalized at 0.55 μm and ρ_{sfc} denotes the surface albedo at solar zenith angle of 60°.

1997]), and $\rho_{(\mu 0=0.5)}$ is the albedo at the solar zenith angle of 60° (Table 1).

3.2. Characterization of Dust Aerosols

[13] Due to the short lifetime (hours to days) and the different sources and chemical reactions during transport of dust aerosols [*Prospero*, 1999; *Savoie et al.*, 1989], the aerosol properties, especially the imaginary part of refractive index and size distribution, show high spatiotemporal variations [*Sokolik et al.*, 1993; *Tegen and Lacis*, 1996]. These variations result in difficulties when quantifying the single scattering albedo (ω_0) of dust aerosols in radiative transfer calculations. Since the direct radiative forcing of dust aerosols is highly sensitive to single scattering albedo (ω_0) [*Liao and Seinfeld*, 1998], much attention has been focused upon studying this parameter [*Kaufman et al.*, 2001a, 2001b; *Haywood et al.*, 2001]. The value of ω_0 at 0.55 μm in recent studies varied from 0.87 [*Haywood et al.*, 2001] to 0.97 [*Kaufman et al.*, 2001a, 2001b; *Moulin et al.*, 2001]. Using light scattering measurements and measured size distributions, *Wang et al.* [2003] have derived an effective ω_0 value of 0.98 (at 0.55 μm) during PRIDE.

[14] The broadband dust aerosol properties used in this study are inferred from the optical properties at 0.55 μm [*Wang et al.*, 2003] and wavelength-dependent extinction cross sections calculated from the SP aerosol optical thickness. Specifically, the Ångström exponent that links the aerosol optical thickness at different wavelengths is first derived from the SP aerosol optical thickness values. The Ångström exponent (α) can be expressed as:

$$\alpha_{(\lambda)} = -\frac{ln\frac{\tau_{(\lambda)}}{\tau_{(\lambda_0)}}}{ln\frac{\lambda}{\lambda_0}}, \lambda_0 = 0.50\mu m \quad (2)$$

where $\tau_{(\lambda)}$ is the aerosol optical thickness value at wavelength λ, and $\alpha_{(\lambda)}$ is the Ångström exponent at wavelength λ and is calculated relative to 0.50 μm. The derived $\alpha(\lambda) = 0.378 - 0.18\lambda$. Our derived α is 0.31 at 0.34 μm and 0.18 at 1.02μm, and is within the range of previous studies (e.g., $0.2 \sim 0.3$) [*Eck et al.*, 1999; *Smirnov et al.*, 2000b; *Reid et al.*, 2003; *Livingston et al.*, 2003]. The Ångström exponent is important for broadband radiative transfer model calculations because it can be used to infer aerosol optical thickness values at different wavelengths when aerosol optical thickness value is available only at a specific wavelength [e.g., *Kato et al.*, 1997]. The extinction cross section β at a wavelength λ can be calculated from

$$\frac{\beta_{(\lambda)}}{\beta_{(0.50)}} = \frac{\tau_{(\lambda)}}{\tau_{(0.50)}} = \left(\frac{\lambda}{0.50}\right)^{-\alpha_{(\lambda)}} \quad (3)$$

[15] *Dubovik et al.* [2002] concluded that the retrieved real part of the dust refractive index from AERONET sky radiance measurements ($1.48 \sim 1.56$) generally agree with available in situ derived values [e.g., *Patterson et al.*, 1977; *Sokolik et al.*, 1993]. However, the imaginary part of refractive index has much lower values ($0.0006 \sim 0.003$) when compared with previous studies [e.g., *Patterson et al.*, 1977]. Therefore, in this study, the real part of the refractive index in each band ($N_{r(\lambda)}$) required in the radiative transfer calculations is the same as that of *Patterson et al.* [1977]. The imaginary part of refractive index for each band $N_{i(\lambda)}$ is derived by adjusting $N_{i(\lambda)}$ until $\beta(\lambda)$ calculated from Mie theory matches the $\beta(\lambda)$ values derived from equation 3. During the calculation of $N_{i(\lambda)}$ from Mie theory, the measured aerosol size distribution is used [*Wang et al.*, 2003]. The derived dust optical properties including wavelength-dependent refractive index $N_{i(\lambda)}$ and $N_{r(\lambda)}$, $\omega_{0(\lambda)}$, asymmetric factor $g_{(\lambda)}$, and normalized $\beta_{(\lambda)}$ over each SW band in the radiative transfer model are listed in Table 1. Our derived broadband ω_0 over the whole visible band is 0.97 that is consistent with the values reported by *Fouquart et al.* [1987]. The derived absorption coefficient also agrees well with the study of *Dubovik et al.* [2002] who inferred a N_i value of $0.0006 \sim 0.003$ and a ω_0 value of 0.98 at 0.67 μm over Cape Verde.

[16] The dust aerosols have irregular shapes and are not spherical [*Kalashnikova and Sokolik*, 2002]. By choosing typical refractive indices and size distributions of naturally occurring dust aerosols, *Mishchenko et al.* [1997] used the T-matrix method to simulate light scattering of dust-like tropospheric aerosols with a shape mixture of randomly oriented polydisperse spheroids. Their results show that the difference in phase function of nonspherical and projected-area-equivalent spherical particles could be large enough to result in errors in the aerosol optical thickness retrievals from radiance measurements [*Mishchenko et al.*, 1997]. However, the difference in the total optical cross section, single scattering albedo and backscattered fraction of spherical and nonspherical particles are much smaller and in most cases do not exceed a few percent indicating that the effect of particle shape on radiative forcing calculations are negligible [*Mishchenko et al.*, 1997].

4. Results and Discussions

[17] The results are organized as follows. We first compared the calculated downward shortwave irradiance (DSWI) at the surface with SMART measurements at Roosevelt Road. We then used the radiative transfer model

to calculate the diurnal dust SWARF both at the surface and top of atmosphere, over the entire study area, by using the GOES 8 AOT670 retrievals [*Wang et al.*, 2003]. Finally, the calculated TOA irradiance are compared with the CERES shortwave irradiance.

4.1. Comparison With SMART Measurements

[18] The SP aerosol optical thickness at 500 nm (hereafter AOT500) and atmospheric sounding profiles are first input into the four-stream radiative transfer model to calculate the DSWI values. Since both SMART and SP measurements were located at Roosevelt Road during PRIDE, the calculated DSWI (including direct, diffuse, and total values) are then compared with the SMART measurements that are within 15 min of SP AOT500 values (total of 3183 points in 22 days). Figure 1 shows the intercomparison between the calculated and the SMART measured downward total, diffuse and direct irradiance. The calculated and measured DSWI are in excellent agreement, with linear coefficients of 0.998, 0.998, 0.962 for total, direct and diffuse irradiance, respectively. The calculated mean and standard deviation values of total, direct and diffuse DSWI are 704 ± 263 W m^{-2}, 559 ± 247 W m^{-2} and 145 ± 55 W m^{-2} respectively, corresponding to measured values of 709 ± 264 W m^{-2}, 549 ± 254 W m^{-2} and 150 ± 66W m^{-2} and are well within the measurement uncertainties [*Ji and Tsay*, 2000]. It is important to note that the direct, diffuse, and total DSWI are measured by three independent instruments. Ideally, although the measured total DSWI should be equal to the measured direct plus measured diffuse DSWI, differences arise due to the cosine response and the dome effect [*Cess et al.*, 2000]. On the basis of independent measurements at the Oklahoma ARM site, *Cess et al.* [2000] reported the sum of the DSWI qualities (total - direct - diffuse) ranges from −2 to −13 W m^{-2}. In this study, the mean value of the sum of the DSWI quantities is about −11 W m^{-2}, that is similar to the values reported by *Cess et al.* [2000]. The ratio of the sum of DSWI to the measured total irradiance is about 1.3% (Table 2) that is also consistent with the study of *Eck et al.* [1998] who also found similar differences between the two independent Eppley PSP pyranometers during SCAR-B. Relevant statistics of the measured and calculated DSWI are listed in Table 2.

[19] Our results do not show large discrepancies between calculated and measured DSWI components that were reported by previous studies (e.g., 32 W m^{-2} discrepancy between calculated and observed values in clear sky regions [*Charlock and Alberta*, 1996]; 34 W m^{-2} discrepancy [*Kato et al.*, 1997]). *Mlawer et al.* [2000] ascribe the discrepancies in the previous studies [e.g., *Kato et al.*, 1997; *Halthore et al.*, 1998] to the uncertainties in characterizing the aerosol properties. Our calculations using aerosol properties of marine type aerosols with the same AOT500 values [*D'Almedia et al.*, 1991] show much larger biases (−15, 8, −17 W m^{-2} for direct, diffuse, and total DSWI respectively) compared to the biases calculated from derived dust aerosol properties in this study. Although, the best fit lines between the calculated and measured diffuse component (Y = 0.8X + 24.6) slightly deviated from the one-to-one fit line, our calculated DSWI values are in excellent agreement with the measured values, implying that the dust aerosols during PRIDE are properly characterized in the radiative transfer model. This is in agreement with the results of *Christopher et al.* [2000] who concluded that when adequate information about aerosol properties is available, the DSWI are in good agreement with measured values at the surface.

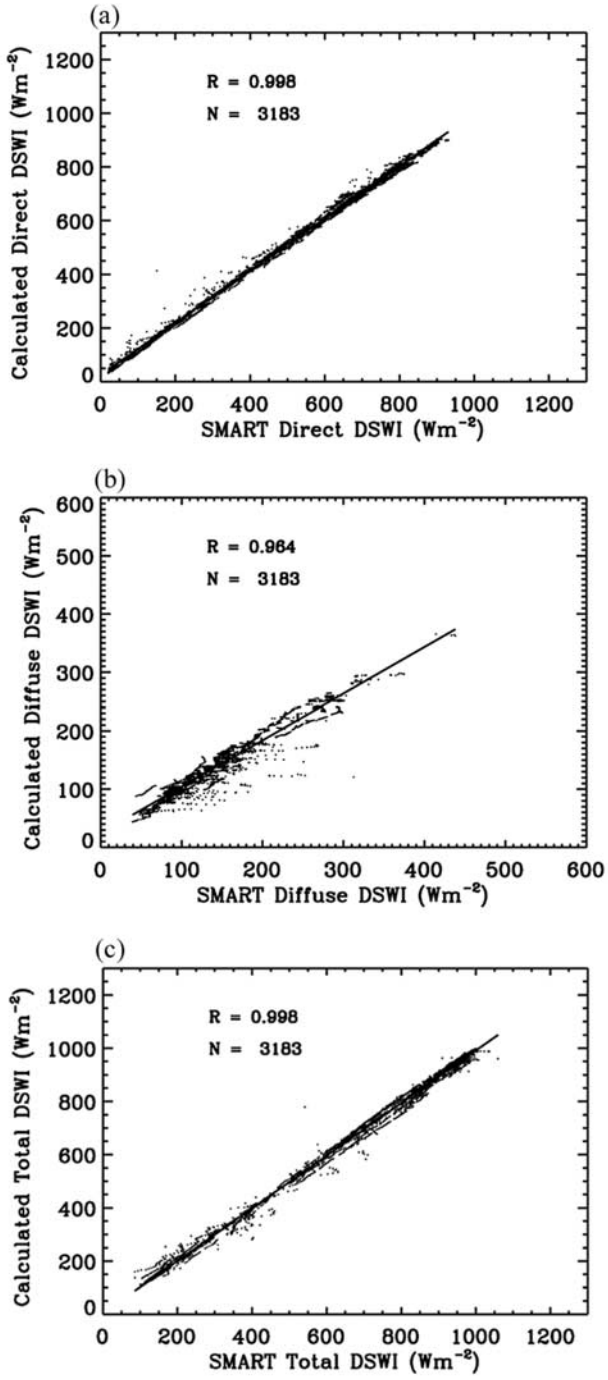

Figure 1. Intercomparison of calculated and SMART measured downward shortwave irradiance (DSWI) for (a) direct (b) diffuse, and (c) total components. The correlation coefficient (R) and the number of data points (N) are also shown. The sold line represents the best fit between calculated and measured fluxes.

[20] As an example, Figure 2 shows the diurnal changes of measured and calculated total DSWI as well as path

Table 2. Statistics of the Comparison Between Modeled and Measured DSWI for 3183 Points[a]

	Mean ± SD	Linear Correlation Coefficient	Linear Fit Equation	RMSE	Bias, W m^{-2}	Bias Percentage
MDR (X)	548.78 ± 254.11	0.99	Y = 0.97 X + 25.24	19.04	10.31	1.8%
CDR (Y)	559.09 ± 247.61					
MDF (X)	150.08 ± 66.10	0.96	Y = 0.8 X + 24.6	20.46	−5.05	−3.3%
CDF (Y)	145.02 ± 55.10					
MTT (X)	708.62 ± 264.42	0.99	Y = 0.99 X + 2.26	19.07	−4.5	−0.5%
CTT (Y)	704.12 ± 262.54					
MTT (X)	708.62 ± 264.42	0.99	Y = 1.00 X − 10.81	12.84	−9.76	−1.3%
MDR + MDF (Y)	698.86 ± 264.94					

[a]MDR, MDF, and MTT denote measured direct, diffuse, and total DSWI, receptively. CDR, CDF, and CTT represent calculated direct, diffuse, and total DSWI. RMSE is root mean square error. Bias is defined as calculated (mean Y) bias to (measured mean X). Bias percentage is defined as bias divided by mean of the measured components.

length [AOT/cos (solar zenith angle)] on 10 July 2000. For display purposes, data are plotted every 5 min. The SP AOT500 varied from 0.32 at 1210 UTC to 0.24 at 1442 UTC, increased to 0.31 at 1600 UTC, and then decreased to 0.17 at 1730 UTC. The measured irradiance changes from 496 W m^{-2} to 996 W m^{-2} and to 985 W m^{-2} in the morning, decreased from 985 W m^{-2} to 962 W m^{-2} at local noon, and continuously decreased to about 203 W m^{-2}. The diurnal variations of AOT are important for accurate calculations of the radiative effect of dust aerosols on the surface because both model calculations and SMART measurements show that the change of 0.1 in optical thickness can lead up to 10 W m^{-2} DSWI change at the surface, depending on solar zenith angles. Therefore the aerosol optical thickness retrieved from geostationary satellites play an important role in estimating DSWI values at the surface.

4.2. SWARF at TOA and Surface During PRIDE

[21] The SWARF of dust aerosols in this study is defined as the difference of shortwave irradiance between dust and background conditions [*Boucher and Tanré*, 2000]. The calculation of SWARF of dust aerosols at the TOA and surface are defined as:

$$\Delta F^{\downarrow}_{toa} = F^{\downarrow}_{toa,dust} - F^{\downarrow}_{toa,bg} \quad (4)$$

$$\Delta F^{\downarrow}_{sfc} = F^{\downarrow}_{sfc,dust} - F^{\downarrow}_{sfc,bg} \quad (5)$$

where $F^{\downarrow}$ denotes the net downward irradiance (downward minus upward irradiance); the subscripts "toa" and "sfc" denote TOA and the surface; and "dust" and "bg" denotes dusty and background conditions, respectively. *Boucher and Tanré* [2000] have shown that the threshold used to define the background conditions is important in the estimation of SWARF both at the surface and TOA [see *Boucher and Tanré*, 2000, Figure 4]. *Liao and Seinfeld* [1998] assume background optical thickness values of 0.05 at 0.55 μm in their model studies. *Kaufman et al.* [2001a, 2001b] examined the background (or baseline) AOT500 over oceans by using 1–3 years of measurements over 10 AERONET stations. Their results show that the background AOT500 value over the Atlantic Ocean is 0.071 [*Kaufman et al.*, 2001a, 2001b]. This value is consistent with the study of *Reid et al.* [2003] who found AOT670 values over dust free regions during PRIDE are always less than 0.08 (corresponding to AOT500 of 0.1) and are representative of clean marine aerosols [*Smirnov et al.*, 2002]. Therefore, to calculate $F^{\downarrow}_{bg}$ in this study, the background is assumed to contain clean marine type aerosols [*D'Almeida et al.*, 1991] with an AOT670 of 0.07.

[22] Using multispectral GOES 8 imager data, and a spatiotemporal detection algorithm, *Wang et al.* [2003] have shown that dust aerosols can be properly identified and aerosol optical thickness can be retrieved during PRIDE. For each noncloudy pixel, GOES 8 AOT670 is used into the radiative model [*Fu and Liou*, 1993] to calculate the $F^{\downarrow}_{dust}$ The SWARF at TOA and surface are then calculated from equations (1) and (2). As an example, Figure 3 show the spatial distribution of GOES 8 AOT670 (Figures 3a–3f), SWARF at TOA (Figures 3g–3l), and the surface SWARF (Figures 3m–3r) of a dust event (19 July ∼ 22 July 2000) during PRIDE. Clouds are shown in black and land areas are denoted in white. The mean AOT670, mean SWARF at TOA and surface at different time periods of this dust event are listed in Table 3. During this dust event, the area mean AOT670 increased by about 0.15 (from 0.17 at 19 July 2000 to 0.33 at 21 July 2000) in about two days. The dust layer started to approach Puerto Rico from the south east (SE) corner of the study area between 19 July 2000 (Figure 3a) and 20 July 2000 (Figure 3b), then moved over Puerto Rico later in the evening (2001 UTC) of 20 July 2000 (Figures 3c and 3d), spread out over the study area on 21 July 2000 (Figure 3e), and finally moved out of the Puerto Rico region on 22 July 2000 (Figure 3f). The highest AOT670 values are found in Figure 4d in the southeast corner of the study area. Under the effect of SE flow, dust aerosols were spread out to the northwest and covered most of the study area (Figure 3e). The spatial distribution of the TOA

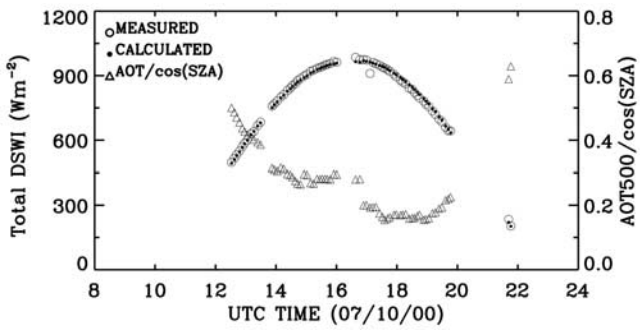

Figure 2. Diurnal variation of measured and calculated total downward short wave irradiance (DSWI) and path length [AOT500/cos(sza)] as a function of UTC time for 10 July 2000.

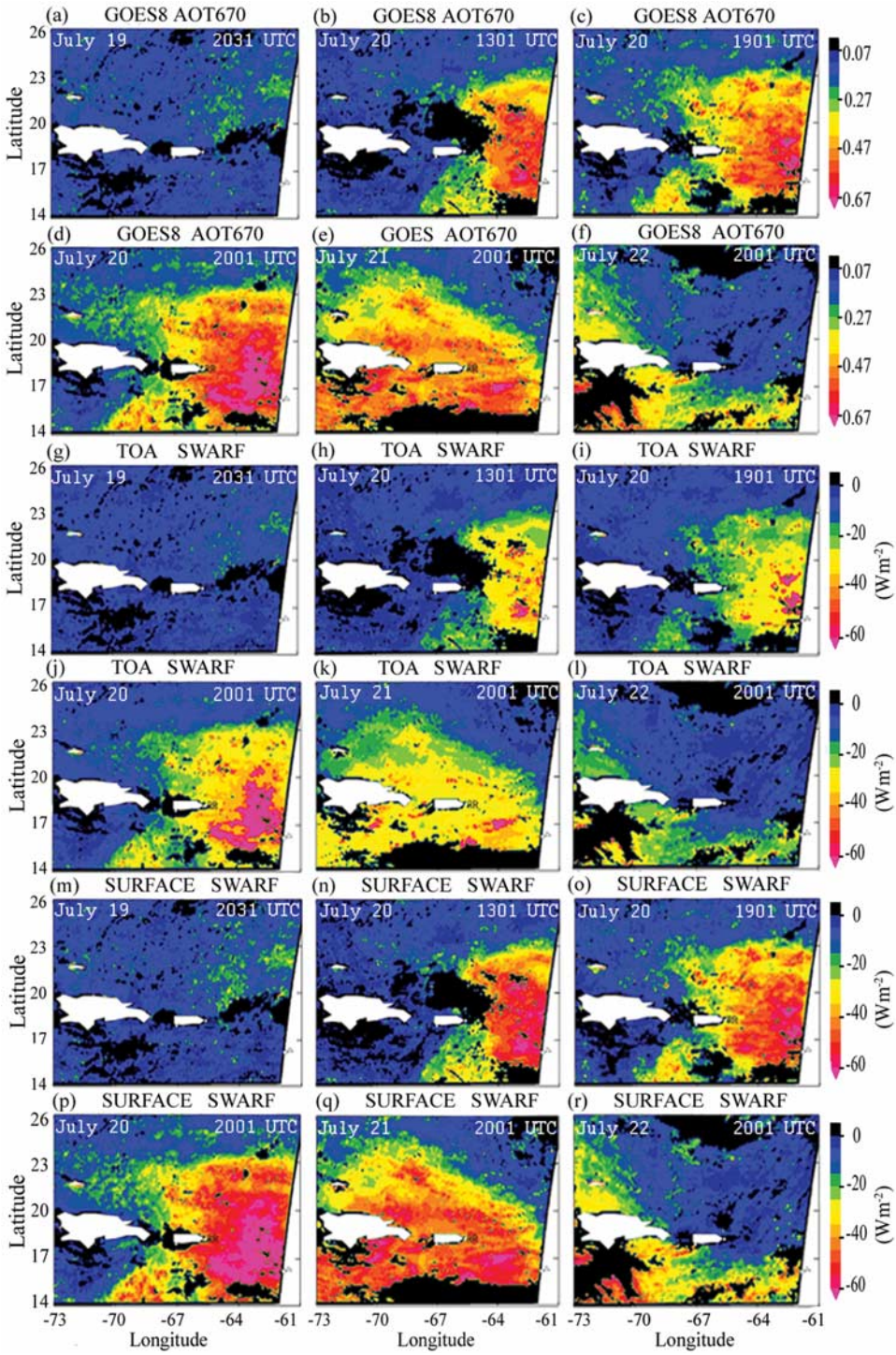

Figure 3. GOES 8 aerosol optical thickness (AOT670) and dust short wave aerosol radiative forcing (SWARF) at the top of atmosphere and the surface for a selected dust event (19–23 July) during PRIDE. Clouds are shown in black and land areas are in white.

Table 3. Statistics of Results for a Selected Dust Event During PRIDE Period[a]

	Time					
Area Mean	19 July 2000, 2031 UTC	20 July 2000, 1301 UTC	20 July 2000, 1901 UTC	20 July 2000, 2001 UTC	21 July 2000, 2001 UTC	22 July 2000, 2001 UTC
AOT	0.17 ± 0.05	0.22 ± 0.15	0.26 ± 0.15	0.30 ± 0.17	0.33 ± 0.17	0.25 ± 0.13
TOA SWARF (W m^{-2})	−7.09 ± 4.22	−10.07 ± 10.35	−11.39 ± 9.66	−16.18 ± 13.01	−18.51 ± 11.95	−12.72 ± 9.18
SURF SWARF (W m^{-2})	−8.62 ± 6.42	−14.10 ± 17.28	−17.70 ± 17.04	−23.38 ± 20.29	−28.03 ± 19.67	−18.49 ± 15.38

[a]AOT denotes optical thickness in study region; SWARF represents shortwave aerosol radiative forcing.

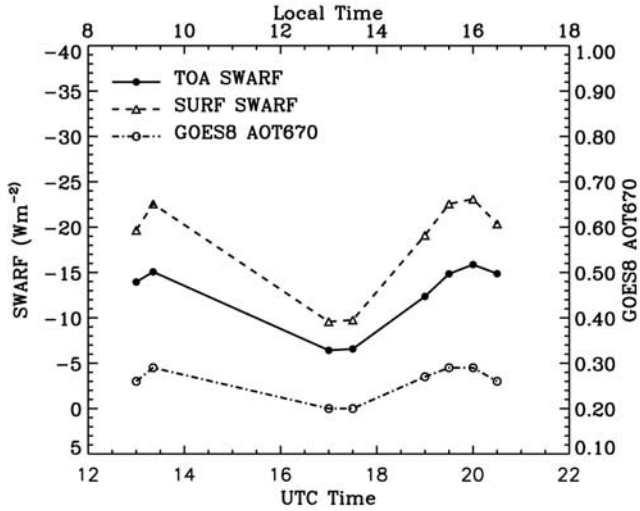

Figure 4. Monthly mean diurnal change of AOT670, TOA SWARF, and surface SWARF during PRIDE. Note the lines in this figure are only used to connect the same symbols and might not represent the actual diurnal cycle at the time periods when GOES 8 retrievals are not available.

SWARF (Figures 3g–3l) and the surface SWARF (Figures 3m–3r) matches the spatial distribution of aerosol optical thickness. This demonstrates how the dust aerosols affect the geographic distribution of radiative energy, where large SWARF always corresponds to large aerosol optical thickness values. Because of the absorption of solar energy by the dust layer, SWARF at surface is always larger than the corresponding top of atmosphere values over oceans under cloud free conditions, depending on solar zenith angle, aerosol optical thickness, surface albedo and aerosol properties [*Liao and Seinfeld*, 1998]. In this case study, the dust event increased the TOA SWARF by about 11 W m^{-2} (from −7 W m^{-2} on 19 July 2000 to −18 W m^{-2} on 21 July 2000) and the surface SWARF by about 20 W m^{-2} (from −8 W m^{-2} on 19 July 2000 to −28 W m^{-2} on 21 July 2000) in two days (Table 3). Another interesting feature is that both the GOES 8 retrievals and SP aerosol optical thickness values have captured large diurnal aerosol optical thickness variations on 20 July 2000 and 21 July 2000 respectively [*Wang et al.*, 2003]. On 21 July 2000, the GOES 8 mean AOT670 in the study region changed from 0.3 in the early morning (1301 UTC) to 0.20 in the late afternoon (1731 UTC) and to 0.31 around 2031UTC. The corresponding mean TOA SWARF on this day changed from −15.95 W m^{-2} to −6.17 W m^{-2} and to −17.95 W m^{-2}, and SWARF at surface changed from −23.66 W m^{-2} to −9.44 W m^{-2} and to −25.54 W m^{-2}, respectively.

[23] The monthly mean diurnal AOT670 and SWARF at the surface and TOA are shown in Figure 4. Since most of the study area was contaminated by Sun glint from 1401 UTC to 1631 UTC and the GOES 8 data at 1801 UTC and 1831 UTC were also not available in our data archive, only results for the remaining eight time periods are shown in the Figure 4. Therefore the lines connecting the points for those times the time periods when GOES 8 retrievals are not available, may not represent the actual aerosol optical thickness and aerosol forcing values. Figure 4 shows that the aerosol optical thickness ranges from 0.20 to 0.30, and are quite uniform except during 1701 and 1731UTC where aerosol optical thickness values are about 0.05 lower than that in other time periods. The SWARF both at surface and TOA closely follows aerosol optical thickness trends, i.e., larger aerosol optical thickness corresponding to larger SWARF. Table 4 is a summary of the results from the model calculations during the PRIDE time period. The monthly averaged AOT670 from GOES 8 retrievals is 0.26 ± 0.13. The monthly averaged SWARF at TOA and surface are −12.34 ± 9.62 W m^{-2} and −18.13 ± 15.81 W m^{-2} respectively. The monthly mean AOT670 retrieved from GOES 8 agrees well with the mean Sun photometer-derived AOT670 values of 0.24 ± 0.11 and 0.27 ± 0.14 at La Paguera and Roosevelt Road during PRIDE, respectively.

[24] Our calculated SWARF of dust aerosols at the TOA at each time period (Table 4) in the Puerto Rico region is small when compared with regions with heavy dust loading near source regions such as the west coast of Africa [e.g., *Haywood et al.*, 2001; *Hsu et al.*, 2000; *Liu et al.*, 2003]. This is due to the small aerosol optical thickness values in the study area (monthly mean value of 0.26, Table 4) when compared with aerosol optical thickness near source regions (a mean AOT670 of 0.4 was reported at Cape Verde during PRIDE period [*Reid et al.*, 2003]). The mean SWARF listed in the third-last column of Table 4 is the daytime mean SWARF for only noncloudy regions during the PRIDE. Furthermore, in our SWARF calculations, we have deducted the effect of the background aerosols. Therefore the mean forcing in Table 4 is called monthly mean daytime clear-sky SWARF [*Boucher and Tanré*, 2000]. Since the GOES 8 imager has one visible channel, assumptions must be made on the chemical composition of aerosols in order to retrieve the column aerosol optical thickness over oceans. Therefore it difficult to directly compare our results with those obtained from other models [e.g., *Haywood et al.*, 1999]. For example, *Haywood et al* [1999] reported that the clear-sky SWARF over global oceans due to different aerosols ranges from −8.7 W m^{-2} to −5.1 W m^{-2} at the TOA and from −10.8 to −7.4 W m^{-2} at the surface for the period 1987–1988. Using AOT retrievals from the POLDER instruments, *Boucher and Tanré* [2000] reported the aerosol radiative perturbation effect (i.e., including background aerosol effect) at TOA over global ocean is nearly constant (∼−5.7 W m^{-2}). However, it is important to note that these SWARF [e.g., *Haywood et al.*, 1999; *Boucher and Tanré*, 2000] over the global oceans are the mean values averaged over day and night. The estimation of monthly daytime "clear sky" SWARF of dust aerosol in this study is the averaged values of instantaneous SWARF over 8 daytime periods. If we divide our SWARF results by a factor by two to compute the monthly "clear sky" SWARF averaged during both day and night, our values are −6.2W m^{-2} at TOA and −9.1W m^{-2} at the surface, that are comparable to the values reported by *Haywood et al* [1999].

[25] We then compare our results with previous studies of global mean SWARF both over land and over oceans. Following the formula by *Charlson et al.* [1991], we divide monthly mean daytime "clear sky" SWARF by a factor of 2 (to average both for day and night) multiplied by the clear sky percentage (66% since cloudy percentage is 34%, Table 4) to get the regional daily averaged "all sky" monthly mean SWARF that is −4.13W m^{-2} at TOA and −6.7 W m^{-2} at the

Table 4. Summary of Results for the Study Period[a]

	Time									
Area Mean	1301 UTC	1331 UTC	1701 UTC	1731 UTC	1901 UTC	1931 UTC	2001 UTC	2031 UTC	Mean[b]	AM Method	PM Method
AOT670	0.26 ± 0.14	0.29 ± 0.14	0.21± 0.10	0.22 ± 0.10	0.27 ± 0.13	0.30 ± 0.14	0.29 ± 0.14	0.27 ± 0.14	0.26 ± 0.13	0.29 ± 0.14	0.29 ± 0.14
Cloud Percentage (%)	33	32	36	35	35	34	34	35	34	32	34
Broadband surface albedo (%)	6.06 ± 0.17	5.81 ± 0.14	5.12 ± 0.03	5.18 ± 0.04	5.54 ± 0.1	5.72 ± 0.12	5.98 ± 0.15	6.27 ±0.18	5.85 ± 0.43	5.81 ± 0.43	5.75± 0.41
TOA SWARF	−3.94 ± 0.54	−15.07 ± 0.84	−6.42 ± 5.14	−6.57 ± 5.13	−12.36 ± 7.97	−14.85 ± 9.39	−15.87 ± 10.38	−14.87 ± 11.16	−12.34 ± 9.81	−14.14 ± 9.80	−14.60 ± 9.70
Surface SWARF	−19.66± 6.71	−22.56 ± 16.57	−9.58 ± 10.41	−9.76 ± 10.25	−19.10 ± 14.36	−22.56 ± 16.11	−23.09 ± 16.82	−20.36 ± 16.92	−18.13 ± 15.99	−21.56 ± 16.34	−22.15 ± 16.09
SZA	48.89 ± 4.14	42.35 ± 4.20	7.39 ± 3.47	13.36 ±3.82	33.72 ± 3.91	40.11 ± 3.63	46.92 ± 3.63	53.74 ± 3.64			
SZA range	38 ∼ 58	32 ∼ 54	0 ∼ 17	5 ∼ 23	26 ∼ 43	33 ∼ 48	39 ∼ 54	46 ∼ 61			
number of images	28	28	28	29	28	23	24	24			

[a]AOT670 denotes aerosol optical thickness, SWARF represents shortwave aerosol radiative forcing (W m^{-2}), and SZA is solar zenith angle.
[b]The mean value of SWARF at eight time periods in one month for noncloudy regions.

surface. The estimate of global dust forcing varies from −0.062W m^{-2} [*Jacobson*, 2001] to −0.25 W m^{-2} [*Tegen et al.*, 1996]. The large regional "all sky" SWARF in our studies (−4.13W m^{-2}) shows that the dust aerosol in the study region in July has an important contribution to the global dust aerosol forcing.

[26] The GOES 8 imager is well suited to capture the diurnal variations of the aerosol optical thickness over large regions. Since the spatial distribution of dust optical thickness can change very quickly in several hours (Figure 3), using only one optical thickness value at one time period to calculate the daily mean SWARF may not be representative. For example, our calculations show if we only use GOES AOT670 at 1331 UTC (local morning, hereafter named AM method) and 1931 (local afternoon, hereafter PM method), our calculated monthly mean SWARF (the last two columns in Table 4) will produce an uncertainty of about 2 W m^{-2} at the TOA and 4 W m^{-2} at the surface when compared to the GOES 8 derived diurnal mean values. These differences could be larger near the dust source regions where the aerosol optical thickness could change by a factor of 2 in less than 2 hours [*Levin et al.*, 1980]. As the spatial distribution of DSWI is closely related to the temperature distribution at the surface and evaporation process in the boundary layer, accurate calculation of DSWI by use of diurnal aerosol optical thickness retrieved from geostationary satellite is important to describe the geographic distributions of radiative fluxes.

4.3. Comparison With CERES and Uncertainty Analyses

[27] Compared to the GOES 8 imager with spatial resolution of about 1X1 km at nadir, the CERES has a larger spatial resolution (20 km × 20 km at nadir) [*Wielicki et al.*, 1996]. To compare the calculated TOA irradiance with CERES derived values, it is necessary to ensure that the collocated CERES footprints have no cloud contamination. However, the CERES ES-8 data set does not account for aerosols and it classifies a dust pixel as either "cloudy" (partly cloudy, mostly cloudy, overcast) or "clear sky". Therefore collocated GOES 8 pixels are used to detect clouds within a CERES footprint. We selected cases where the observational time differences between the GOES 8 and CERES is less than 15 min in non-Sun glint regions for noncloudy pixels based on the GOES 8 dust detection algorithm [*Wang et al.*, 2003]. A total of 147 points fit these criteria (Figure 5), and most of these points (about 70%) are on June 28th on which the heaviest dust event was reported with daily mean AOT670 of about 0.5 [*Reid et al.*, 2003]. Figure 5 shows the comparison between the CERES and calculated TOA irradiance. The solid and dotted curves in this Figure 5 are the curves simulated using the gompertz function ($y = a_1 a_2^{a} 3^{x} + a_4$) to fit the CERES and modeled TOA irradiance respectively, which implies that the calculated TOA irradiance is about 10 W m^{-2} larger than the mean CERES irradiance. The CERES ES-8 data does not have specific aerosol models when converting the measured radiances to irradiance values. *Chou et al* [2002] reported that the monthly mean CERES TOA irradiance underestimated modeled irradiance by about 3 ∼ 6 W m^{-2} in the Puerto Rico region [see *Chou et al.*, 2002, Figure 7]. However, *Ackerman and Chung*

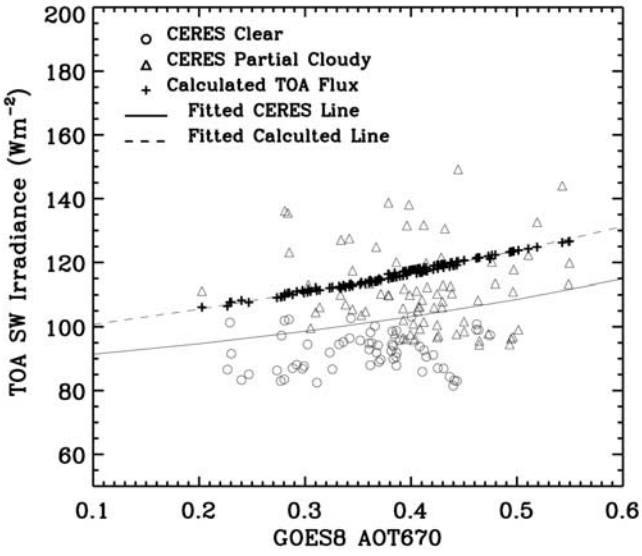

Figure 5. Comparison between CERES and calculated TOA irradiance. The solid and dotted curves are the curves simulated using gompertz function ($y = a_1 a_2 a_3^x + a_4$) to fit the CERES and modeled TOA fluxes respectively. For CERES, a_1, a_2, a_3, and a_4 are 16.07, 2.65, 1.66, and 72.47, respectively. For modeled flux, a_1, a_2, a_3, and a_4 are 31.87, 2.23, 1.4, and 62.66, respectively.

[1992] found that the ERBE derived irradiance overestimated their calculations in their study region where aerosol optical thickness ranged from 0.5 to 1.5. One possible reason is that the CERES could misclassify Saharan dust with high aerosol optical thickness as partial cloudy or most cloudy [*Ackerman and Chung*, 1992], thereby overestimating the shortwave (SW) irradiance; while aerosols with low aerosol optical thickness are classified as clear sky, thereby underestimating the irradiance. Therefore accurate aerosol ADMs are needed to reliably estimate SWARF from broadband satellite measurements.

[28] Besides the uncertainties of dust nonspherical effect, uncertainties in ocean surface albedo (ρ) could also contribute to errors in SWARF calculations. The mean surface albedo in this study is 5.85% (Table 4). In this study we calculate the surface albedo (ρ) by use of the empirical formula (equation (1)) from *Dickinson* [1983] and albedo values at solar zenith angle of 60° ($\rho_{(0.5)}$, Table 1) from *Charlock et al* [1997]. The uncertainties of surface albedo in this study might result from the parameterization of solar zenith angle in equation (1) and the initial values of $\rho_{(0.5)}$ that could be affected by changes in wind speeds over the ocean [*Burt*, 1954]. *Wang et al* [2003] discuss the uncertainties of ocean albedo ($\Delta\rho$) is about 0.4% $\sim$ 0.6%. We thereby made a relative change of 5% ($\Delta\rho/\rho$) to evaluate the SWARF uncertainties from $\Delta\rho$. Our sensitivity studies show the surface SWARF uncertainties are limited to 1.2 W m^{-2} and TOA SWARF uncertainties are limited to 0.2 W m^{-2} for a mean AOT670 of 0.26 in PRIDE (Table 4).

5. Summary

[29] This study is among the first to estimate the daytime diurnal variation of dust AOT and SWARF both at TOA and surface over low dust-loading regions using GOES 8 imager data. Using measured and derived aerosol properties as well as the Sun photometer aerosol optical thickness and GOES 8 aerosol optical thickness retrievals, a broadband radiative transfer model is used to calculate the shortwave radiative irradiance both at the TOA and at the surface. The results can be summarized as follows.

[30] 1. There is excellent agreement between calculated and measured downward shortwave irradiance values at the surface. Although previous studies have indicated discrepancies between the measured and calculated irradiance at the surface, our results show that when aerosols are well characterized in radiative transfer models, there is good agreement between the measured and calculated irradiances. Therefore accurate characterization of aerosols are critical for studies that attempt to model the radiative energy budget of the Earth-atmosphere system.

[31] 2. Our calculated TOA shortwave irradiance overestimated CERES irradiance by about 10 W m^{-2}. Preliminary analysis shows that this discrepancy is largely due to the misclassification of dust aerosols by the CERES ES-8 algorithm and the lack of aerosol angular dependence models (ADMs) for dust aerosols. The new CERES instruments on Terra and Aqua can be used to develop ADMs that will further reduce uncertainties in TOA aerosol radiative forcing estimates.

[32] 3. The dust aerosols in the Puerto Rico region during the summer months is an important contributor to the global dust SWARF, with a diurnal mean SWARF of -12.34 ± 9.62 W m^{-2} at TOA and -18.13 ± 15.81 W m^{-2} at the surface, implying that the transport of dust aerosols from the Saharan desert result in a large-scale shortwave radiative cooling effect, affecting the regional climate in downwind areas (like Puerto Rico) thousands of miles from the dust source.

[33] 4. Although the calculated values in this study are comparable with previous studies, our study shows that the spatial distribution of SWARF at TOA and DSWI at the surface may not be well represented in models that utilize the aerosol optical thickness retrievals from one time period during the day. This could result in uncertainties of 2 W m^{-2} at the TOA and 4 W m^{-2} at the surface in the estimation of SWARF in the Puerto Rico region, and possibly larger uncertainties near the dust source regions where diurnal variation of dust loading is expected to be large. This result underscores the importance of using geostationary satellites for aerosol research.

[34] 5. Our analysis shows uncertainties in this study are about 0.2W m^{-2} and 1.2 W m^{-2} in the calculation of SWARF at the TOA and at surface respectively, mainly due to the uncertainties in ocean surface albedos.

[35] Although this study shows the advantages and importance of characterizing aerosol properties from ground-based instruments in satellite retrievals, our current method has been used only over the oceans. However recent studies have demonstrated the potential of geostationary imagers for retrieving smoke aerosol optical thickness over land [*Zhang et al.*, 2001; *Christopher and Zhang*, 2002; *Knapp et al.*, 2002]. The techniques developed in this study will be applicable for the next generation of geostationary satellites such as Meteosat Second Generation (MSG) [*Schmetz et al.*, 2002] to provide geographic distribution of radiative

irradiance with high temporal and spatial resolutions. Our results indicate that highly valuable information can be derived from geostationary imagers that are complementary to information derived from polar orbiting satellites. However, further studies are necessary to develop and refine aerosol retrievals both over land and ocean to examine the impact of aerosols on the Earth-atmosphere system.

[36] **Acknowledgments.** This research was partially supported by NASA grant NCC 8141 (Global Aerosol Climatology Project), NASA's IDS program (FLAMBE) and was part of Jun Wang's master's thesis. We thank Gary Jedlovec for the GOES 8 data, U. S. Nair for providing the GOES calibration algorithms; Q. Fu and K.-N. Liou for the four stream radiative transfer model and Fred Rose for guidance in using the model. The CERES data were obtained from the NASA-Earth Observing and Information System, Distributed Active Archive Center (DAAC) at the Langley Research Center.

References

Ackerman, S. A., and M. Chung, Radiative effects of airborne dust on regional energy budgets at the top of Atmosphere, *Notes Corr.*, *31*, 223–233, 1992.

Ackerman, S. A., and S. K. Cox, The Saudi Arabian heat low: Aerosol distribution and thermodynamic structure, *J. Geophys. Res.*, *87*, 8991–9002, 1982.

Boucher, O., and D. Tanré, Estimation of the aerosol perturbation to the Earth's radiative budget over oceans using POLDER satellite retrievals, *Geophys. Res. Lett.*, *27*, 1103–1106, 2000.

Burt, W. V., Albedo over wind-roughed water, *J. Atmos. Sci.*, *11*, 283–290, 1954.

Cess, R. D., T. Qian, and M. Sun, Consistency tests applied to the measurements of total, direct and diffuse shortwave radiation at the surface, *J. Geophys. Res.*, *105*, 24,881–24,887, 2000.

Charlock, T. P., and T. L. Alberta, The CERES/ARM/GEWEX Experiment (CAGEX) for the retrieval of radiative irradiance with satellite data, *Bull. Am. Meteorol. Soc.*, *77*, 2673–2693, 1996.

Charlock, T. P., F. G. Rose, D. A. Rutan, T. L. Alberta, D. P. Kratz, L. H. Coleman, N. M. Smith, and T. D. Bess, CERES algorithm theoretical basis document, Subsystem 5.0, Compute Surface and Atmospheric Fluxes, NASA Langley Research Center, Hampton, Va., 1997. (Available at http://asd-www.larc.nasa.gov/ATBD/pdf_docs/r2_2/ceres-atbd2.2-s5.0.pdf).

Charlson, R. J., J. Langner, C. B. Leovy, and S. G. Warren, Perturbation of the Northern Hemisphere radiative balance by backscattering from anthropogenic sulfate aerosols, *Tellus, Ser. AB*, *43*, 152–163, 1991.

Chou, M.-D., P.-K. Chan, and M. Wang, Aerosol radiative forcing derived from SeaWiFS—Retrieved aerosol optical properties, *J. Atmos. Sci.*, *39*, 748–757, 2002.

Christopher, S. A., and J. Zhang, Daytime variation of shortwave direct radiative forcing of biomass burning aerosols from GOES 8 imager, *J. Atmos. Sci.*, *59*, 681–691, 2002.

Christopher, S. A., X. Li, R. M. Welch, J. S. Reid, P. V. Hobbs, T. F. Eck, and B. Holben, Estimation of surface and top-of-atmosphere (TOA) shortwave irradiance in biomass-burning regions during SCAR-B, *J. Appl. Meteorol.*, *39*, 1742–1753, 2000.

Claquin, T., M. Schulz, Y. J. Balkanski, and O. Boucher, Uncertainties in assessing radiative forcing by mineral dust, *Tellus, Ser. B*, *50*, 491–505, 1998.

D'Almeida, G. A., P. Koepke, and E. P. Shettle, *Atmospheric Climatology and Radiative Characteristics*, A. Deepak, Hampton, Va., 1991.

Dickinson, R. E., Land surfaces processes and climate—Surface albedos and energy balance, *Adv. Geophys.*, *25*, 305–353, 1983.

Dubovik, O., B. Holben, T. F. Eck, A. Smirnov, Y. J. Kaufman, M. D. King, D. Tanré, and I. Slutsker, Variability of absorption and optical properties of key aerosol types observed in worldwide locations, *J. Atmos. Sci.*, *59*, 590–608, 2002.

Eck, T. F., B. N. Holben, I. Slutsker, and A. Setzer, Measurements of irradiance attenuation and calculations of aerosol single scattering albedo for biomass burning aerosols in Amazonia, *J. Geophys. Res.*, *103*, 31,865–31,878, 1998.

Eck, T. F., B. N. Holben, J. S. Reid, O. Dubovik, A. Smirnov, N. T. O'Neill, D. Tanré, I. Slutsker, and S. Kinne, Wavelength dependence of the optical depth of biomass burning, urban, and desert dust aerosol, *J. Geophys. Res.*, *104*, 31,333–31,350, 1999.

Fouquart, Y., B. Bonnel, G. Bogniez, J. C. Buriez, L. Smith, J. J. Morcrette, and A. Cerf, Observations of Sahara aerosols, results of ECLATS field experiment, part II: Broadband radiative characteristics of the aerosols and vertical radiative flux divergence, *J. Clim. Appl. Meteorol.*, *26*, 38–52, 1987.

Fu, Q., and K. N. Liou, Parameterization of the radiative properties of cirrus clouds, *J. Atmos. Sci.*, *50*, 2008–2025, 1993.

Halthore, R. N., S. Nemesure, S. E. Schwartz, D. G. Imrie, A. Berk, E. G. Dutton, and M. H. Bergin, Models overestimate diffuse clear sky irradiance: A case for excess atmospheric absorption, *Geophys. Res. Lett.*, *25*, 3591–3594, 1998.

Hansen, J. E., and A. A. Lacis, Sun and dust versus greenhouse gases: An assessment of their relative roles in global climate change, *Nature*, *346*, 713–719, 1990.

Haywood, J. M., V. Ramaswamy, and B. J. Soden, Tropospheric aerosol climate forcing in clear-sky satellite observations over the oceans, *Science*, *283*, 1299–1303, 1999.

Haywood, J. M., P. N. Francis, M. D. Glew, and J. P. Taylor, Optical properties and direct radiative effect of Saharan dust: A case study of two Saharan dust outbreaks using aircraft data, *J. Geophys. Res.*, *106*, 18,417–18,430, 2001.

Holben, B. N., et al., AERONET—A federal instrument network and data archive for aerosol characterization, *Remote Sens. Environ.*, *66*, 1–16, 1998.

Hsu, N. C., J. R. Herman, and C. Weaver, Determination of radiative forcing of Saharan dust using combined TOMS and ERBE data, *J. Geophys. Res.*, *105*, 20,649–20,662, 2000.

Intergovernmental Panel on Climate Change (IPCC), *Climate Change 2001: The Scientific Basis, Contribution of Working Group I to the Third Assessment Report of the Intergovernmental Panel on Climate Change*, edited by J. T. Houghton et al., Cambridge Univ. Press, New York, 2001.

Jacobson, M. Z., Global direct radiative forcing due to multicomponent anthropogenic and natural aerosols, *J. Geophys. Res.*, *106*, 1551–1568, 2001.

Ji, Q., and S.-C. Tsay, On the dome effect of Eppley pyrgeometers and pyranometers, *Geophys. Res. Lett.*, *27*, 971–974, 2000.

Kalashnikova, O. V., and I. N. Sokolik, Importance of shapes and compositions of wind-blown dust particles for remote sensing at solar wavelengths, *Geophys. Res. Lett.*, *29*(10), doi:10.1029/2002GL014947, 2002.

Karyampudi, et al., Validation of the Saharan dust plume conceptual model using lidar, Meteosat, and ECMWF data, *Bulletin Am. Meteorol. Soc.*, *80*, 1045–1075, 1999.

Kato, S., T. P. Ackerman, E. E. Clothiaux, J. H. Mather, G. G. Mace, M. L. Wesely, F. Murcray, and J. Michalsky, Uncertainties in modeled and measured clear-sky surface shortwave irradiances, *J. Geophys. Res.*, *102*, 25,881–25,898, 1997.

Kaufman, Y. J., D. Tanré, O. Dubovik, A. Karnieli, and L. A. Remer, Absorption of sunlight by dust as inferred from satellite and ground-based remote sensing, *J. Geophys. Lett.*, *28*, 1479–1482, 2001a.

Kaufman, Y. J., A. Smirnov, B. N. Holben, and O. Dubovik, Baseline maritime aerosol: methodology to derive the optical thickness and scattering properties, *Geophys. Res. Lett.*, *28*, 3251–3254, 2001b.

Knapp, K. R., T. H. Vonder Haar, and Y. J. Kaufman, Aerosol optical depth retrieval from GOES-8: Uncertainty study and retrieval validation over South America, *J. Geophys. Res.*, *107*(D7), 4055, doi:10.1029/2001JD000505, 2002.

Konzelmann, T., D. R. Cahoon, and C. H. Whitlock, Impact of biomass burning in equatorial Africa on the downward surface shortwave irradiance: Observations versus calculations, *J. Geophys. Res.*, *101*, 22,833–22,844, 1996.

Legrand, M., G. Gautenet, and J. C. Buriez, Thermal impact of Saharan dust over land, part II: Application to satellite IR remote sensing, *J. Appl. Meteorol.*, *31*, 181–193, 1992.

Levin, Z., J. H. Joseph, and Y. Mekler, Properties of Sharav (Khamsin) dust—Comparison of optical and direct sampling data, *J. Atmos. Sci.*, *27*, 882–891, 1980.

Levy, R., L. A. Remer, D. Tanre, Y. J. Kaufman, C. Ichoku, B. Holben, J. Livingston, P. B. Russell, and H. Maring, Evaluation of the MODIS retrievals of dust aerosol over the ocean during PRIDE, *J. Geophys. Res.*, *108*, doi:10.1029/2002JD002460, in press, 2003.

Liao, H., and J. H. Seinfeld, Radiative forcing by mineral dust aerosols: Sensitivity to key variables, *J. Geophys. Res.*, *103*, 31,637–31,645, 1998.

Liou, K. N., Q. Fu, and T. P. Ackerman, A simple formulation of the delta-four-stream approximation for radiative transfer parameterizations, *J. Atmos. Sci.*, *45*, 1940–1947, 1988.

Liu, X., J. Wang, and S. A. Christopher, Shortwave direct radiative forcing of Saharan dust aerosols over the Atlantic Ocean, *Int. J. Remote Sens*, in press, 2003.

Livingston, J. M., et al., Airborne Sun photometer measurements of aerosol optical depth and columnar water vapor during the Puerto Rico Dust Experiment and comparison with land, aircraft, and satellite measurements, *J. Geophys. Res.*, *108*, doi:10.1029/2002JD02520, in press, 2003.

McClatchey, R. A., R. W. Fenn, J. E. A. Selby, F. E. Volz, and J. S. Garing, optical properties of the atmosphere, *Rep. AFCRL-TR-71-0279*, *Environ. Res. Pap. 354*, Air Force Cambridge Res. Lab., Bedford, Mass., 1971.

McPeters, R. D., and G. J. Labow, An assessment of the accuracy of 14.5 years of Nimbus 7 TOMS version 7 ozone data by comparison with the Dobson network, *Geophys. Res. Lett.*, *23*, 3695–3698, 1996.

Mishchenko, M. I., L. D. Travis, R. A. Kahn, and R. A. West, Modeling phase functions for dust-like tropospheric aerosols using a shape mixture of randomly oriented polydisperse spheroids, *J. Geophys. Res.*, *102*, 16,831–16,847, 1997.

Mlawer, E. J., P. D. Brown, S. A. Clough, L. C. Harrison, J. J. Michalsky, and P. W. Kiedron, Comparison of spectral direct and diffuse solar irradiance measurements and calculations for cloud-free conditions, *Geophys. Res. Lett*, *27*, 2653–2656, 2000.

Moulin, C., H. R. Gordon, V. F. Banzon, and R. H. Evans, Assessment of Sahara dust absorption in the visible from SeaWiFS imagery, *J. Geophys. Res.*, *106*, 18,239–18,250, 2001.

Patterson, E. M., D. A. Gillette, and B. H. Stockton, Complex index of refraction between 300 nm and 700 nm for Sahara aerosols, *J. Geophys. Res.*, *82*, 3153–3160, 1977.

Penner, J. E., R. E. Dickinson, and C. A. O'Neill, Effects of aerosol from biomass burning on the global radiation budget, *Science*, *256*, 1432–1434, 1992.

Prospero, J. M., Long-term measurements of the transport of African minerals dust to the southeastern United States: Implications for regional air quality, *J. Geophys. Res.*, *104*, 15,917–15,927, 1999.

Rao, C. R. N., L. L. Stowe, and E. P. McClain, Remote sensing of aerosols over the ocean using AVHRR data: Theory, practice and applications, *Int. J. Remote Sens.*, *10*, 743–749, 1989.

Reid, J. S., et al., Analysis of measurements of Saharan dust by airborne and ground-based remote sensing methods during the Puerto Rico Dust Experiment (PRIDE), *J. Geophys. Res.*, *108*, doi:10.1029/2002JD002493, in press, 2003.

Savoie, D. L., J. M. Prospero, and E. S. Saltzman, Non-sea-salt sulfate and nitrate in trade wind aerosols at Barbados: evidence for long-range transport, *J. Geophys. Res.*, *94*, 5069–5080, 1989.

Schmetz, J., P. Pili, S. Tjemkes, D. Just, J. Kerkmann, S. Rota, and A. Ratier, An introduction to Meteosat second generation (MSG), *Bull. Amer. Meteorol. Soc.*, *81*, 977–1001, 2002.

Smirnov, A., B. N. Holben, T. F. Eck, O. Dubovik, and I. Slutsker, Cloud screening and quality control algorithms for the AERONET data base, *Remote Sens. Environ.*, *73*, 337–349, 2000a.

Smirnov, A., B. N. Holben, D. Savoie, J. M. Prospero, Y. J. Kaufman, D. Tanré, T. F. Eck, and I. Slutsker, Relationship between column aerosol optical thickness and in situ ground based dust concentrations over Barbados, *Geophys. Res. Lett.*, *27*, 1643–1646, 2000b.

Smirnov, A., B. N. Holben, Y. J. Kaufman, O. Dubovik, T. F. Ecl, I. Slutsker, C. Pietras, and R. N. Halthore, Optical properties of atmospheric aerosol in maritime enviroments, *J. Atmos. Sci.*, *59*, 501–523, 2002.

Sokolik, I. N., and O. B. Toon, Direct radiative forcing by anthropogenic airborne mineral aerosol, *Nature*, *381*, 681–683, 1996.

Sokolik, I. N., A. Andronova, and T. C. Johnson, Complex refractive index of atmospheric dust aerosols, *Atmos. Environ.*, *27*, 2495–2502, 1993.

Tegen, I., and A. A. Lacis, Modeling of particle size distribution and its influence on the radiative properties of mineral dust aerosol, *J. Geophys. Res.*, *101*, 19,237–19,244, 1996.

Tegen, I., A. Lacis, and I. Fung, The influence of mineral aerosols from disturbed soils on climate forcing, *Nature*, *380*, 419–422, 1996.

Trautmann, T., and M. A. Box, Fast yet accurate net flux calculation for realistic atmosphere with variable aerosol loadings, *J. Geophys. Res.*, *100*, 1081–1092, 1995.

Twomey, S. A., The influence of pollution on the short wave albedo of clouds, *J. Atmos. Sci*, *34*, 1149–1152, 1977.

Wang, J., S. A. Christopher, J. S. Reid, H. Maring, D. L. Savoie, B. Holben, J. Livingston, P. B. Russell, and S.-K. Yang, GOES 8 retrieval of dust aerosol optical thickness over the Atlantic Ocean during PRIDE, *J. Geophys. Res.*, *108*, doi:10.1029/2002JD002494, in press, 2003.

Wielicki, B. A., B. R. Barkstrom, E. F. Harrison, R. B. Lee III, G. L. Smith, and J. E. Cooper, Clouds and the Earth's Radiant Energy System (CERES): An Earth observing system experiment, *Bull. Am. Meteorol. Soc.*, *77*, 853–868, 1996.

Zhang, J., S. A. Christopher, and B. Holben, Intercomparison of aerosol optical thickness derived from GOES 8 imager and ground-based Sun photometers, *J. Geophys. Res.*, *106*, 7387–7398, 2001.

S. A. Christopher and J. Wang, Department of Atmospheric Sciences, University of Alabama in Huntsville, Huntsville, AL 35805, USA. (sundar@nsstc.uah.edu; wangjun@nsstc.uah.edu)

Q. Ji, SSAI, NASA Goddard Space Flight Center, Greenbelt, MD 20771, USA. (ji@climate.gsfc.nasa.gov)

S.-C. Tsay, Laboratory for Atmospheres, NASA Goddard Space Flight Center, Greenbelt, MD 20771, USA. (tsay@climate.gsfc.nasa.gov)